Biomaterials Science

ROYAL SOCIETY OF CHEMISTRY

PAPER

View Article Online
View Journal

Cite this: DOI: 10.1039/d5bm01181g

Collagen IV-targeted phase-change nanoparticles illuminate early liver fibrosis staging *via* ultrasound molecular imaging

Yan Long, †[a,b] Shigen Zhong, †[c] Fang Li,[d] Wei Zhang,[a] Yaqin Hu,[a] Mingyuan Dai,[a] Min Zheng,[a] Long Cheng*[a] and Haitao Ran *[a]

Early non-invasive diagnosis of liver fibrosis remains a significant clinical challenge. This study aimed to develop type IV collagen-targeted phase-change nanoparticles (AC-IV-PFP@NPs) for ultrasound molecular imaging (UMI), allowing accurate staging of early-stage liver fibrosis. AC-IV-PFP@NPs were prepared by conjugating anti-collagen IV antibody (AC-IV) to perfluoropentane-encapsulated liposomes *via* carbodiimide coupling. Physicochemical properties were characterized using transmission electron microscopy, dynamic light scattering, and confocal microscopy. In CCl_4-induced fibrotic rats representing METAVIR stages S0–S4, the targeted nanoparticles were administered intravenously. The nanoparticles displayed spherical morphology with a mean diameter of 307.92 ± 4.16 nm, high AC-IV conjugation efficiency (78.94 ± 2.83%), and a favorable biosafety profile (cell viability >87% at 6 mg mL^{-1}). Targeting specificity was validated both *in vitro* and *in vivo*, with fluorescence imaging showing a 3.8-fold increase in binding to fibrotic collagen IV relative to non-targeted controls ($P < 0.001$). CEUS signal intensity peaked at 30 min post-injection and showed a strong positive correlation with the fibrosis stage ($r = 0.725$, $P < 0.001$). ROC analysis demonstrated high diagnostic accuracy for early fibrosis: an area under the curve (AUC) of 0.949 for distinguishing S0 from S1–S4 (sensitivity 85.5%, specificity 91.7%) and an AUC of 0.923 for separating S0–S1 from S2–S4 (sensitivity 90.7%, specificity 79.2%). To date, AC-IV-PFP@NPs represent the first type IV collagen-targeted UMI platform for liver fibrosis staging in rats, offering non-invasive, real-time assessment with high sensitivity for early-stage disease (S1–S2). This approach addresses the limitations of biopsy and conventional imaging and offers a promising and transformative approach for clinical fibrosis management.

Received 8th August 2025,
Accepted 2nd November 2025

DOI: 10.1039/d5bm01181g

rsc.li/biomaterials-science

Introduction

Liver fibrosis, a common pathological consequence of chronic liver disease (CLD), is a critical precursor to cirrhosis and hepatocellular carcinoma, contributing to over 1 million deaths annually worldwide.[1,2] Accurate staging of liver fibrosis is essential for clinical decision-making, as timely intervention can halt or even reverse disease progression.[3] Liver biopsy remains the gold standard for diagnosis, but its invasiveness, risk of complications, sampling variability, and poor patient acceptance significantly limit its application.[4,5]

Non-invasive diagnostic alternatives also have limitations. Serological markers such as FIB-4 show low specificity due to interference from concurrent inflammatory processes.[6] Conventional imaging methods, including computed tomography (CT) and magnetic resonance imaging (MRI), display low sensitivity for early-stage fibrosis and are further limited by radiation exposure or poor accessibility in resource-limited settings.[7,8] Ultrasound elastography is widely used but demonstrates limited sensitivity and specificity and cannot differentiate inflammation from early fibrotic changes.[9,10] A diagnostic gap remains in detecting early liver fibrosis, where collagen deposition is minimal but potentially reversible with intervention.[11]

In recent years, nanoparticle-based strategies have gained significant attention as promising tools for the targeted diag-

[a]*Department of Ultrasound and Chongqing Key Laboratory of Ultrasound Molecular Imaging and Therapy, the Second Affiliated Hospital of Chongqing Medical University, Chongqing 400010, People's Republic of China.*
E-mail: 304188@hospital.cqmu.edu.cn, ranhaitao@hospital.cqmu.edu.cn
[b]*Department of Health Management Centre, Chongqing General Hospital, Chongqing University, Chongqing 401147, People's Republic of China*
[c]*Department of Ultrasound, Chongqing General Hospital, Chongqing University, Chongqing 401147, People's Republic of China*
[d]*Department of Cardiology, the Second Affiliated Hospital of Chongqing Medical University, Chongqing 400010, People's Republic of China*
†These authors contributed equally to this work and shared the first authorship.

nosis of liver fibrosis. These approaches primarily employ molecular markers characteristic of key pathogenic components, such as integrin αvβ3 and platelet-derived growth factor receptor-β (PDGFR-β) expressed on activated hepatic stellate cells (HSCs), and collagen I within the extracellular matrix (ECM).[12] However, ultrasonic molecular imaging nanoprobes specifically targeting type IV collagen (Col IV) have rarely been described. Although Col IV-targeted nanoparticles have been developed for other pathological conditions, such as atherosclerosis,[13] their potential application in liver fibrosis remains unexplored. Given that Col IV is deposited early in the course of fibrosis, its targeted detection may provide higher diagnostic sensitivity compared with existing molecular imaging strategies.

Col IV has been identified as a promising biomarker for early fibrosis.[14] As a structural component of basement membranes, Col IV synthesis increases in the initial phase of fibrogenesis before the accumulation of collagen types I and III.[15,16] Although serum Col IV assays show diagnostic potential, they cannot spatially localize fibrotic lesions, reducing their value for precise staging.[17] Ultrasound molecular imaging (UMI) allows real-time, non-invasive visualization of molecular targets.[7] However, conventional microbubbles are limited by their short vascular half-life (<10 min), inability to extravasate, lack of extracellular matrix (ECM)-specific targeting, and inability to penetrate dense fibrotic tissue due to their size (>500 nm).[18]

To address these limitations, collagen IV-targeted phase-change nanoparticles (AC-IV-PFP@NPs) were developed (Fig. 1A). This system includes three elements: (1) active targeting *via* anti-collagen IV antibody (AC-IV) conjugation, enabling specific recognition of Col IV within fibrotic ECM; (2) phase-transition capability using a perfluoropentane (PFP) core that undergoes low-intensity focused ultrasound (LIFU)-triggered vaporization into microbubbles, amplifying contrast-enhanced ultrasound (CEUS) signals at fibrotic sites;[19] and (3) enhanced permeability and retention (EPR) effect enabled by sub-400 nm size, allowing passage through disrupted vascular endothelium in fibrotic tissue.[20]

This study presents the first application of UMI using Col IV-targeted nanoprobes for liver fibrosis staging in a rat model (Fig. 1B). Targeting specificity was confirmed *in vitro* and *in vivo*, with an excellent biosafety profile of AC-IV-PFP@NPs. CEUS signal intensity strongly correlated with METAVIR stages (S0–S4), supporting the quantitative capability of this approach. Diagnostic performance for early-stage fibrosis was high, with an area under the curve (AUC) of 0.949 in distinguishing S0 from S1–S4. Mechanistic analysis of late-stage signal attenuation indicated spatial shielding of Col IV by dense collagen I/III that physically blocks nanoparticle access, leading to a relative decrease in Col IV abundance.[21] This platform associates molecular targeting with clinical imaging, offering a non-invasive and accurate method for fibrosis staging, including the previously challenging early stages. Improved detection of early fibrosis may allow earlier therapeutic intervention and better patient outcomes.

Materials and methods

Materials

Lipid components included 1,2-dipalmitoyl-*sn-glycero*-3-phosphocholine (DPPC), 1,2-distearoyl-*sn-glycero*-3-phosphorylglycerol (DSPG) (Avanti Polar Lipids, USA), NH_2-PEG_{5000}-DSPE (DSPE-PEG_{2000}-NH_2) (Xi'an Ruixi Biotechnology, China), and cholesterol (CH) (Sigma-Aldrich, USA). The targeting ligand anti-collagen IV antibody (AC-IV) and its FITC-conjugated form (AC-IV-FITC) were obtained from Sigma-Aldrich (USA). Liquid perfluoropentane (PFP) (Aladdin, China) served as the phase-change core. Fluorescent tags included 1,1′-dioctadecyl-3,3,3′,3′-tetramethylindocarbocyanine perchlorate (DiI) (Beyotime, China) and 4′,6-diamidino-2-phenylindole (DAPI) (Solarbio, China). Conjugation reagents included 2-(*N*-morpholino)ethanesulfonic acid (MES buffer), 1-ethyl-3-(3-dimethylaminopropyl)carbodiimide (EDC), and *N*-hydroxysuccinimide (NHS) (Sigma-Aldrich, USA).

Synthesis of AC-IV-PFP@NPs

Preparation of NH_2-PFP@NPs. To form a lipid film, a mixture of DPPC, DSPE-PEG_{2000}-NH_2, DSPG, and CH in a 20 : 7 : 3 : 4 mass ratio was dissolved in 15 mL of chloroform. The solvent was evaporated using a rotary evaporator (RE-52A, Yarong, China) at 45 °C for 30 min with continuous rotation (60 rpm), producing a uniform lipid film. For hydration and sonication, the dried film was hydrated with 6 mL of PBS (pH 7.4) and mixed with 200 μL PFP. The resulting suspension was sonicated on ice (4 °C) using a probe sonicator (Scientz-II, China) under pulsed conditions (5 s on/5 s off, 45% amplitude) for a total of 3 min. The suspension was purified by centrifugation at 8000 rpm for 5 min at 4 °C (Eppendorf 5430R, Germany), and the pellet was resuspended in PBS to yield NH_2-functionalized phase-change nanoparticles (NH_2-PFP@NPs).[20]

AC-IV conjugation. Conjugation of AC-IV-COOH to NH_2-PFP@NPs was carried out using carbodiimide chemistry.[22] For antibody activation, 600 μL AC-IV (1 mg mL^{-1}) was incubated with EDC/NHS (mass ratio 8 : 3) in 0.1 M MES buffer (pH 5.2) at 25 °C for 2 h with shaking. The pH of the activated solution was then adjusted to 8.0 using NaOH, followed by the addition of NH_2-PFP@NPs. The conjugation reaction was carried out overnight at 4 °C with shaking (200 rpm). Conjugated nanoparticles were isolated by centrifugation at 8000 rpm for 5 min at 4 °C and washed three times with PBS to remove unbound antibodies. For fluorescence labeling, DiI was added during lipid film formation, and AC-IV was substituted with AC-IV-FITC.

Nanoparticle characterization

Dynamic light scattering (DLS; Zetasizer Nano ZS90, Malvern, UK) was used at 25 °C to determine particle size and zeta potential, with measurements conducted in triplicate. Nanoparticle morphology was assessed by low-voltage transmission electron microscopy (LV-TEM; Tecnai G2 12, FEI, USA). The morphology of the lyophilized AC-IV-PFP@NPs was

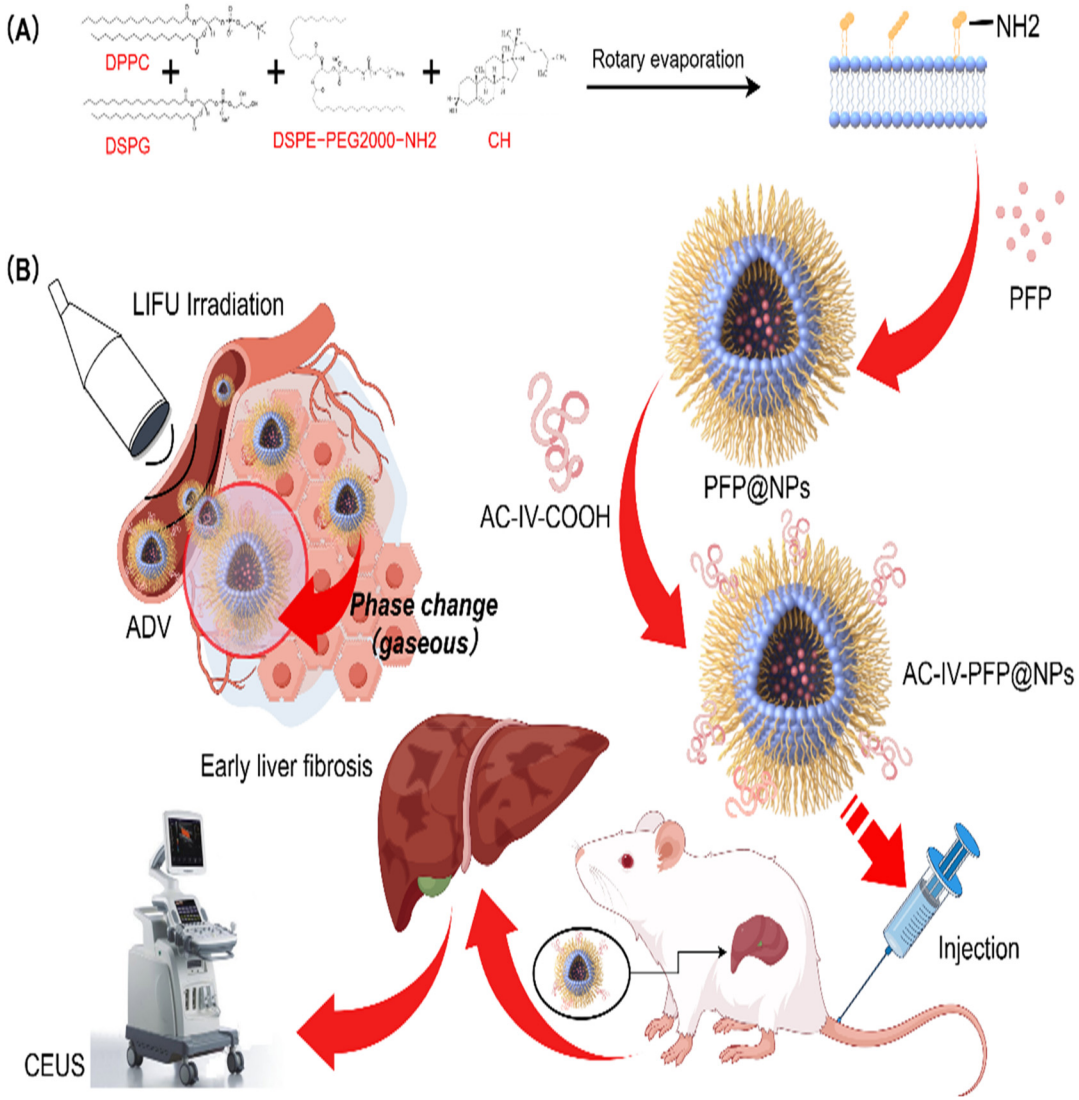

Fig. 1 Contrast-enhanced ultrasound (CEUS) imaging of AC-IV-PFP@NPs targeting liver fibrosis in rats. (A) Schematic representation of the synthesis and delivery of AC-IV-PFP@NPs. Following caudal vein injection, the nanoparticles (NPs) circulated through the capillary interstitium and accumulated in fibrotic liver tissue *via* collagen-targeting by the AC-IV peptide. (B) Liver fibrosis visualization using the CEUS model after low-intensity focused ultrasound (LIFU)-induced acoustic droplet vaporization (ADV) of the nanoparticles. Abbreviations: DPPC, 1,2-dipalmitoyl-*sn*-*glycero*-3-phosphocholine; DSPG, 1,2-distearoyl-*sn*-*glycero*-3-phosphorylglycerol; DSPE-PEG2000-NH_2, amino-modified PEGylated 1,2-dioctadecanoyl-*sn*-*glycero*-3-phosphoethanolamine; CH, cholesterol; CEUS, contrast-enhanced ultrasound; PFP, perfluoropentane; LIFU, low-intensity focused ultrasound; ADV, acoustic droplet vaporization.

observed using scanning electron microscopy (SEM; CLARA, TESCAN, Czechia). Nanoparticle stability was evaluated over 14 days at 4 °C using DLS. To evaluate colloidal stability under physiological conditions, particle size, the polydispersity index (PDI), and zeta potential were monitored for 14 days at 37 °C in a 1 : 6 dilution of 10% serum-containing cell culture medium using DLS. Targeting efficiency was visualized *via* confocal laser scanning microscopy (CLSM; Leica TCS SP8, Germany). DiI and FITC were excited/emitted at 549/565 nm and 488/525 nm, respectively. Flow cytometry (FACSCalibur, BD, USA) was used to quantify AC-IV conjugation efficiency. *In vitro* phase-transition experiments were conducted by suspending AC-IV-PFP@NPs in gel molds and exposing them to low-intensity focused ultrasound (LIFU) at varying power intensities (1, 2, and 3 W cm^{-2}) for 0, 1, 2, 3, 4, and 5 min. The LIFU parameters included an ultrasonic frequency of 650 kHz ± 10% and focal lengths of 28 ± 15 mm and 12.5 ± 15 mm for the first and second treatment heads, respectively. Morphological changes following ultrasound exposure were observed and recorded by optical microscopy.

SPR measurements. The surface plasmon resonance (SPR) analysis was conducted using an OpenSPR™ instrument (Nicoya) to characterize the binding interaction between AC-IV and Col IV. AC-IV was immobilized on a sensor chip *via* stan-

dard 1-ethyl-3-(3-dimethylaminopropyl)carbodiimide/*N*-hydroxysuccinimide (EDC/NHS) coupling chemistry. Col IV was diluted in the same analytical buffer to prepare seven concentrations (500, 250, 125, 62.5, 31.3, 15.6, and 7.81 nM). All binding assays were performed at a flow rate of 20 μL min^{-1}, with both association and dissociation phases recorded in the analysis buffer. Each concentration was analyzed sequentially in ascending order. Sensor surface regeneration was achieved using 10 mM glycine–HCl buffer at a flow rate of 150 μL min^{-1}. After regeneration and complete removal of bound analytes, the chip was reused for subsequent analyses under identical surface conditions.

Biocompatibility assessment

***In vitro* cytotoxicity.** BRL-3A rat hepatocytes were cultured in DMEM supplemented with 10% fetal bovine serum (FBS). The cells were treated with AC-IV-PFP@NPs at concentrations ranging from 0.187 to 6 mg mL^{-1} for 24 h. Cell viability was assessed using the CCK-8 assay. Briefly, 10 μL of the CCK-8 reagent was added to each well, followed by incubation at 37 °C for 2 h. Absorbance was measured at 450 nm using a microplate reader (BioTek Synergy H1, USA).

***In vivo* biosafety.** Healthy female Sprague–Dawley rats (200–220 g, n = 6) were randomly assigned to two groups: saline control and AC-IV-PFP@NPs (6 mg mL^{-1}, 1 mL, administered *via* tail vein). Blood samples were collected at 1, 24, and 48 h post-injection for complete blood count (CBC) and serum biochemistry, including Alanine Aminotransferase (ALT), Aspartate Aminotransferase (AST), Blood Urea Nitrogen (BUN), and Creatinine (Cr), using an automated hematology analyzer (Mindray BC-2800vet, China). Major organs (heart, liver, spleen, lungs, and kidneys) were harvested at 48 h, fixed in 4% paraformaldehyde, paraffin-embedded, sectioned, and stained with H&E for histological evaluation.

Liver fibrosis models and imaging

Female Sprague–Dawley rats (8 weeks old, 200 ± 20 g) were obtained from the Chongqing Medical University Animal Center. All procedures were approved by the Institutional Animal Care and Use Committee (IACUC-CQMU-2024-01037). Liver fibrosis was induced *via* intraperitoneal injection of 40% CCl_4 in olive oil (0.3 mL per 100 g body weight), administered twice per week. Control animals (n = 12) received the vehicle only. Experimental groups were treated for 3, 5, 7, 9, or 11 weeks (n = 12 per group).[23]

Biodistribution and metabolism of AC-IV-PFP@NPs

Rats with liver fibrosis were injected *via* the tail vein with AC-IV-PFP@NPs labeled with 1,1′-dioctadecyl-3,3,3′,3′-tetramethylindotricarbocyanine iodide (DiR). Major organs, including the heart, liver, spleen, lungs, and kidneys, were collected for fluorescence imaging using an *in vivo* imaging system (IVIS; PerkinElmer, UK) at 0.25, 0.5, 1.0, 1.5, 2.0, 4.0, 12.0, and 24 h after injection. To assess the pharmacokinetics, healthy SD rats were injected with DiR-labeled AC-IV-PFP@NPs (1 mL, 6 mg mL^{-1}). Blood samples were obtained at 5, 15, and 30 min and at 1.0, 1.5, 2.0, 4.0, 6.0, 8.0, 12.0, and 24 h post-injection. Fluorescence imaging was performed using IVIS, and all images were analyzed using Living Image software (PerkinElmer).[20]

In vivo ultrasound imaging

AC-IV-PFP@NPs or non-targeted PFP@NPs (6 mg mL^{-1}, 1 mL) were administered *via* the tail vein. At 30 min post-injection, LIFU (3 W cm^{-2}, 3 min; Vevo LAZR, Fujifilm, Japan) was applied to the liver to induce phase transition. B-mode and CEUS imaging were conducted at 15, 30, 45, 60, and 90 min post-injection using a high-frequency linear array transducer (MX250, 21 MHz). Echo intensity was quantified using DFY software (Chongqing Medical University). The detailed imaging parameters are summarized in Table S4.

Histopathological validation

Liver tissues were fixed in 4% paraformaldehyde, paraffin-embedded, and sectioned at 5 μm. Standard H&E staining was used for general histology. Masson's trichrome staining was applied to detect collagen deposition (blue), while Picrosirius red (PSR) staining was used for collagen fiber visualization under polarized light. The percentage of the collagen-positive area was quantified as the Masson-positive area divided by the total tissue area using ImageJ v1.53. Fibrosis staging was conducted using the METAVIR system by a pathologist with over 20 years of experience: S0, no fibrosis; S1, portal fibrosis without septa; S2, portal fibrosis with few septa; S3, numerous septa without cirrhosis; and S4, cirrhosis.

Statistical analysis

All data were expressed as mean ± standard deviation (mean ± SD) and analyzed using SPSS 27.0 (SPSS Inc., Chicago, IL, USA). Normality was assessed using the Shapiro–Wilk test. Group comparisons were conducted using the Mann–Whitney U test (two groups) or the Kruskal–Wallis test (more than two groups). Spearman's rank correlation was used for correlation analysis. Diagnostic performance was evaluated using receiver operating characteristic (ROC) curves and the corresponding AUC. The inter-observer agreement was assessed using the intraclass correlation coefficient (ICC). The significance thresholds were: $^{*}P < 0.05$; $^{**}P < 0.01$; $^{***}P < 0.001$; and $^{****}P < 0.0001$.

Results

Synthesis and characterization of AC-IV-PFP@NPs

AC-IV-PFP@NPs were successfully synthesized using rotary evaporation–phacoemulsification, and carbodiimide-mediated antibody conjugation. LV-TEM confirmed the formation of spherical particles with an average diameter of 295 ± 3.52 nm, consistent with DLS measurements showing a mean size of 307.92 ± 4.16 nm (Fig. 2A and C). SEM images showed that most nanoparticles are spherical with smooth surfaces (Fig. 2B). The size was slightly greater than that of non-targeted PFP@NPs (290.36 ± 6.95 nm, Fig. 2E). Successful surface modification was further supported by a significant change in

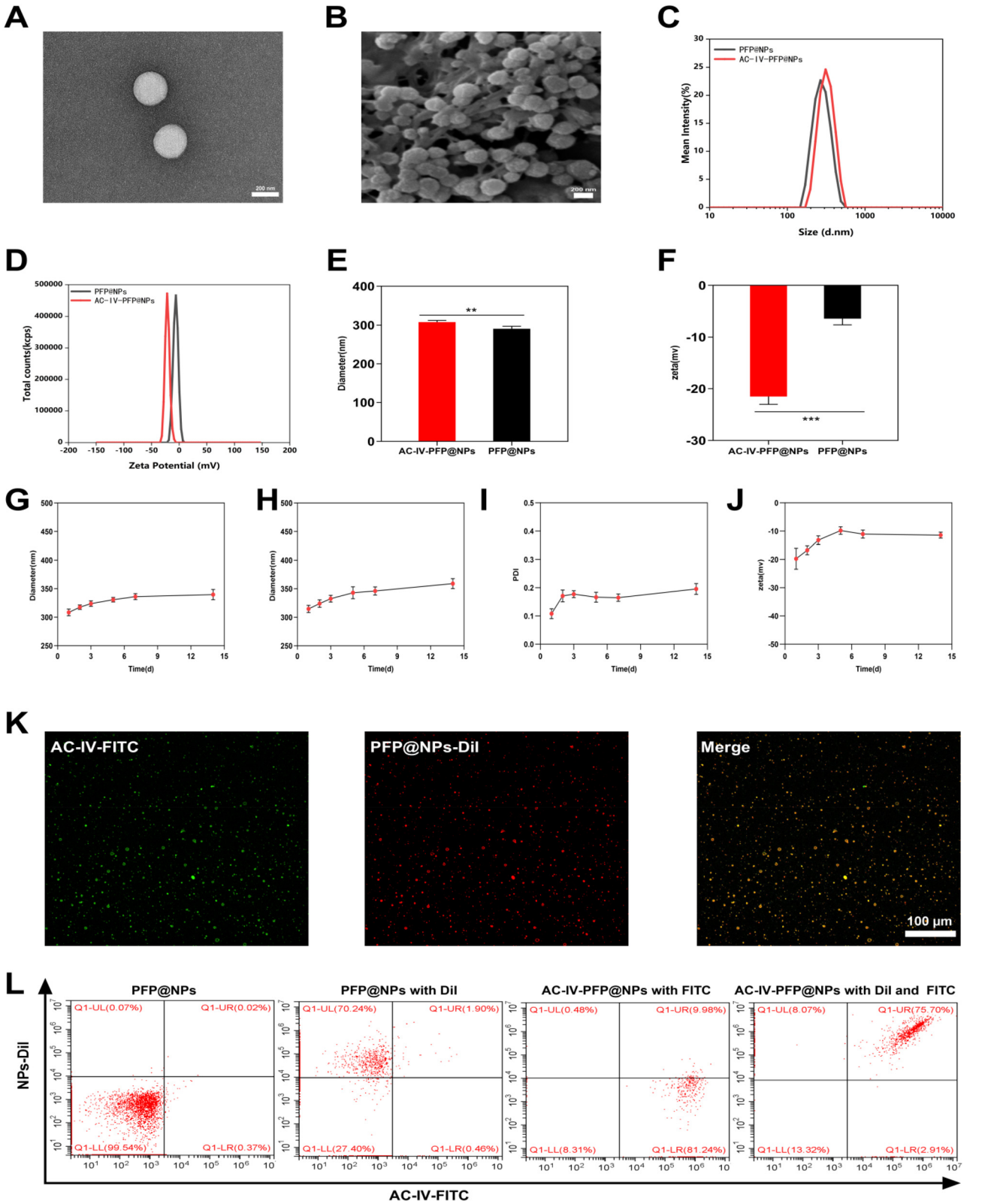

Fig. 2 Physicochemical characterization of AC-IV-PFP@NPs. (A) Low-voltage transmission electron microscopy image of AC-IV-PFP@NPs (scale bar: 200 nm). (B) Scanning electron microscopy image of AC-IV-PFP@NPs (scale bar: 200 nm). (C) Particle size distribution profiles of AC-IV-PFP@NPs and PFP@NPs. (D) Zeta potential distribution of AC-IV-PFP@NPs and PFP@NPs. (E and F) Comparative analysis of the particle size and zeta potential between AC-IV-PFP@NPs and PFP@NPs. (G) Stability of the particle size at 4 °C over 14 days. (H–J) Stability of particle size, PDI, and zeta potential in 10% serum-containing cell culture medium at 37 °C over 14 days. (K) Confocal laser scanning microscopy images showing dual fluorescence labeling of AC-IV-PFP@NPs: red (Dil in liposomes) and green (FITC in AC-IV) (scale bar: 100 μm). (L) Flow cytometry analysis showing the percentage of dual-labeled AC-IV-PFP@NPs.

the zeta potential from −6.41 ± 1.21 mV (PFP@NPs) to −21.52 ± 2.63 mV following AC-IV conjugation ($P < 0.001$, Fig. 2D and F). This change in particle size and potential reflects the introduction of negatively charged functional groups from antibody binding to the nanoparticle surface.

Nanoparticle stability was evaluated under different conditions. After 14 days at 4 °C, the particle diameter increased by less than 10%, indicating good storage stability (Fig. 2G). When incubated in a 10% serum-containing cell culture medium at 37 °C for 14 days, the particle size ranged from 308 to 360 nm (Fig. 2H) and the PDI remained between 0.1 and 0.2 (Fig. 2I), suggesting good colloidal stability of the nanoparticles. The zeta potential increased from −20 to −11 mV (Fig. 2J), likely due to sequential adsorption of serum proteins, initially cationic species that mask surface negative charges, followed by opsonization with anionic proteins.[24] These findings are essential for *in vivo* applications where nanoparticle integrity affects systemic circulation and biodistribution.

Fluorescence labeling validated the successful and uniform antibody conjugation. CLSM images showed colocalization of DiI (a lipophilic membrane dye emitting red fluorescence) and FITC-labeled AC-IV (green fluorescence), confirming the simultaneous incorporation of the lipid marker and the targeting ligand (Fig. 2K). Flow cytometry analysis demonstrated a conjugation efficiency of 78.94 ± 2.83% (Fig. 2L), indicative of high coupling yield. These physicochemical properties are essential for ensuring effective biodistribution and target engagement within the complex microenvironment of fibrotic liver tissue, where EPR facilitates passive accumulation, while active targeting enhances specific binding to type IV collagen. *In vitro* phase-transition experiments demonstrated that the nanoparticle size reached its maximum after 3 min of irradiation with 3 W cm^{-2} LIFU (Fig. S1).

Biocompatibility evaluation of AC-IV-PFP@NPs

The biocompatibility of AC-IV-PFP@NPs was assessed through both *in vitro* and *in vivo* approaches. In the *in vitro* cytotoxicity assay, BRL-3A rat hepatocytes showed over 87% viability following 24 h exposure to nanoparticles across a concentration range of 0.187–6 mg mL^{-1}, with no statistically significant differences compared to the PBS control group ($P > 0.05$; Fig. 3A). These results indicate minimal cytotoxicity under experimental conditions. *In vivo* biosafety was evaluated in healthy Sprague-Dawley rats intravenously injected with 6 mg mL^{-1} AC-IV-PFP@NPs (1 mL). Hematological and biochemical analyses performed at 1, 24, and 48 h post-injection revealed no significant alterations in CBC or serum markers including ALT, AST, BUN, and Cr ($P > 0.05$; Fig. 3B). Histological examination of major organs (heart, liver, lungs, spleen, and kidneys) using H&E staining demonstrated no evidence of acute toxicity or morphological damage (Fig. 3C). Together, these findings confirm the biosafety of AC-IV-PFP@NPs, supporting their potential for clinical translation as targeted ultrasound contrast agents for non-invasive liver fibrosis staging. The absence of systemic or organ-specific toxicity addresses key safety considerations for future diagnostic imaging applications.

Establishment of animal models

In the control group, all 12 rats remained healthy throughout the experiment, exhibiting normal feeding behavior, progressive weight gain, and a shiny coat. Rats in the experimental group showed significant reductions in food intake, lethargy, weight loss, and dull, oily fur. Among the experimental animals, 55 successfully developed the liver fibrosis model, while 5 rats died at various time points between weeks 5 and 11 of the CCL_4 administration period, likely due to its hepatotoxicity. Based on the Metavir scoring system, fibrosis staging of the successfully modeled rats revealed 12 cases in stage S1, 14 in stage S2, 13 in stage S3, and 16 in stage S4. All 12 control rats were classified as stage S0, indicating normal hepatic histology without fibrosis.

Collagen-targeting ability of AC-IV-PFP@NPs

The H&E staining of fibrotic rat liver tissues showed moderate to severe hepatocellular edema, with a loose, lightly stained, and vacuolated cytoplasm. Some hepatocytes displayed ballooning degeneration. PSR staining highlighted fibrotic regions in red, while Masson's trichrome staining highlighted these areas in blue, together confirming the presence of liver fibrosis (Fig. 4A). The binding affinity between AC-IV and collagen IV was evaluated using SPR. Biacore X100 analysis demonstrated a dissociation constant (KD) of 7.39×10^{-8} M, indicating strong and specific binding between AC-IV and Col IV (Fig. S2).

In healthy rats, DiR-labeled AC-IV-PFP@NPs exhibited a pharmacokinetic half-life of 1.07 ± 0.20 h in circulation (Fig. 4B), suggesting their suitability as contrast agents due to rapid systemic clearance. In fibrotic rats, biodistribution analysis revealed significantly higher fluorescence intensity in the liver compared to other organs, with peak accumulation observed at 1 h ($49.63 \pm 8.62 \times 10^7$) followed by a rapid decline. By 24 h post-injection, the fluorescence intensity in all organs decreased below 2×10^7 (Fig. 4C, D and S3).

The targeting capability of AC-IV-PFP@NPs to collagen IV was validated through *in vitro* and *in vivo* assays. Incubation of DiI/FITC-labeled AC-IV-PFP@NPs with fresh cryosections of fibrotic livers (5 weeks after CCl_4 administration) led to significantly higher fluorescence signals in fibrotic areas compared to sections treated with rat IgG-PFP@NPs and non-targeted PFP@NPs (29.36 ± 2.00 *vs.* 7.12 ± 2.05 *vs.* 6.87 ± 2.13; $P < 0.001$; Fig. 4E). Similarly, in *in vivo* experiments, liver sections collected 30 min after intravenous injection of AC-IV-PFP@NPs displayed significantly higher fluorescence accumulation in fibrotic regions than those treated with rat IgG-PFP@NPs and non-targeted particles (25.97 ± 1.98 *vs.* 6.94 ± 1.72 *vs.* 6.77 ± 1.43; $P < 0.001$; Fig. 4F). This enrichment is attributed to the high affinity of AC-IV for type IV collagen, a basement membrane component upregulated during early fibrogenesis, enabling specific localization to fibrotic ECM.[14,16]

For competitive binding confirmation, DiI/FITC-labeled AC-IV-PFP@NPs were pre-incubated with excess soluble Col IV (1 mg mL^{-1}) for 30 min before exposure to fibrotic liver cryo-

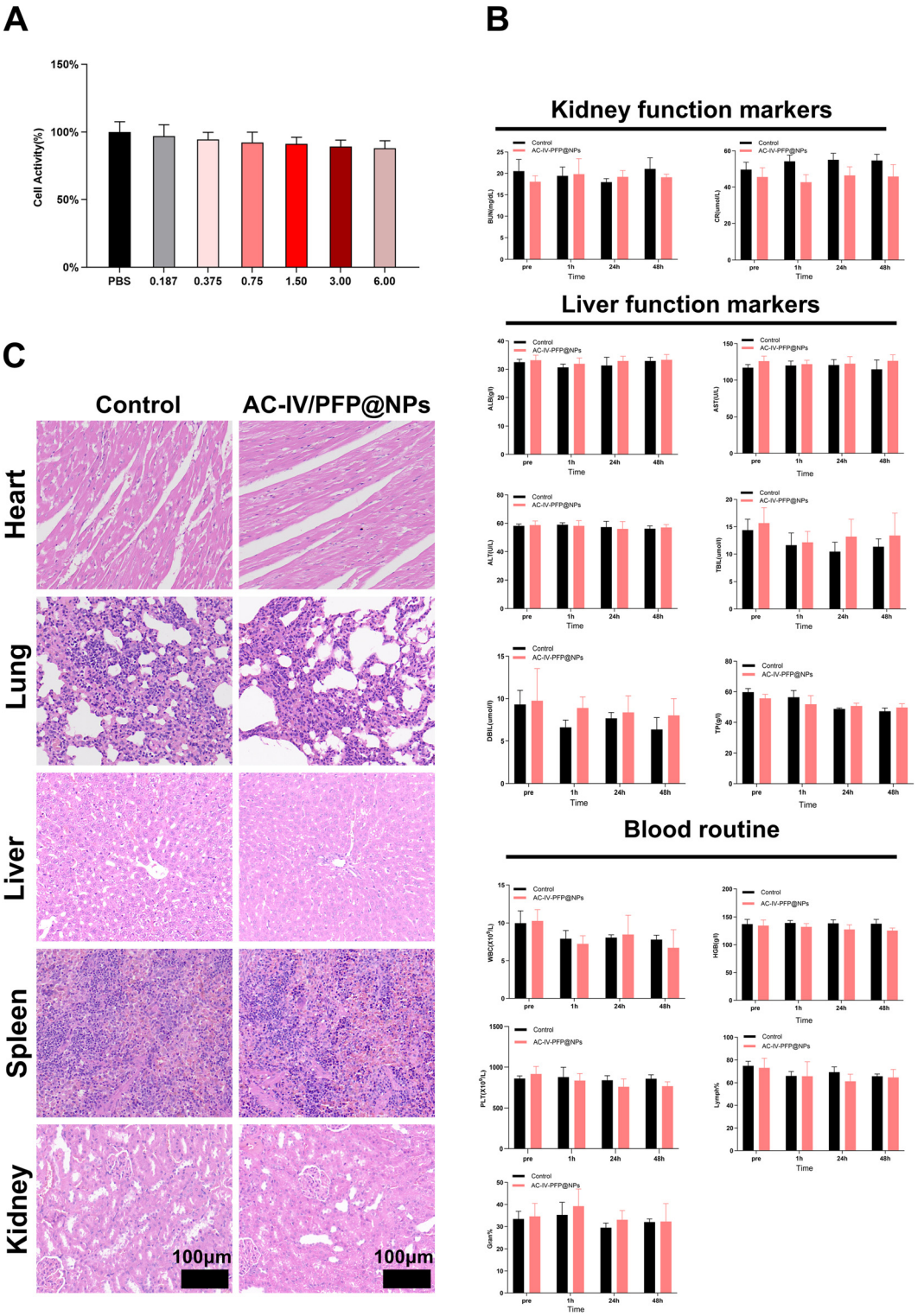

Fig. 3 *In vitro* and *in vivo* biosafety assessment of AC-IV-PFP@NPs. (A) CCK-8 assay results showing BRL-3A cell viability after exposure to varying concentrations of AC-IV-PFP@NPs. (B) Hematological and serum biochemical parameters in healthy rats following administration of saline (control) or AC-IV-PFP@NPs (n = 3 per group). (C) Histological examination of major organs (H&E staining) from saline- or AC-IV-PFP@NP-treated healthy rats (n = 3). Scale bar: 100 μm. Data are presented as mean ± SD.

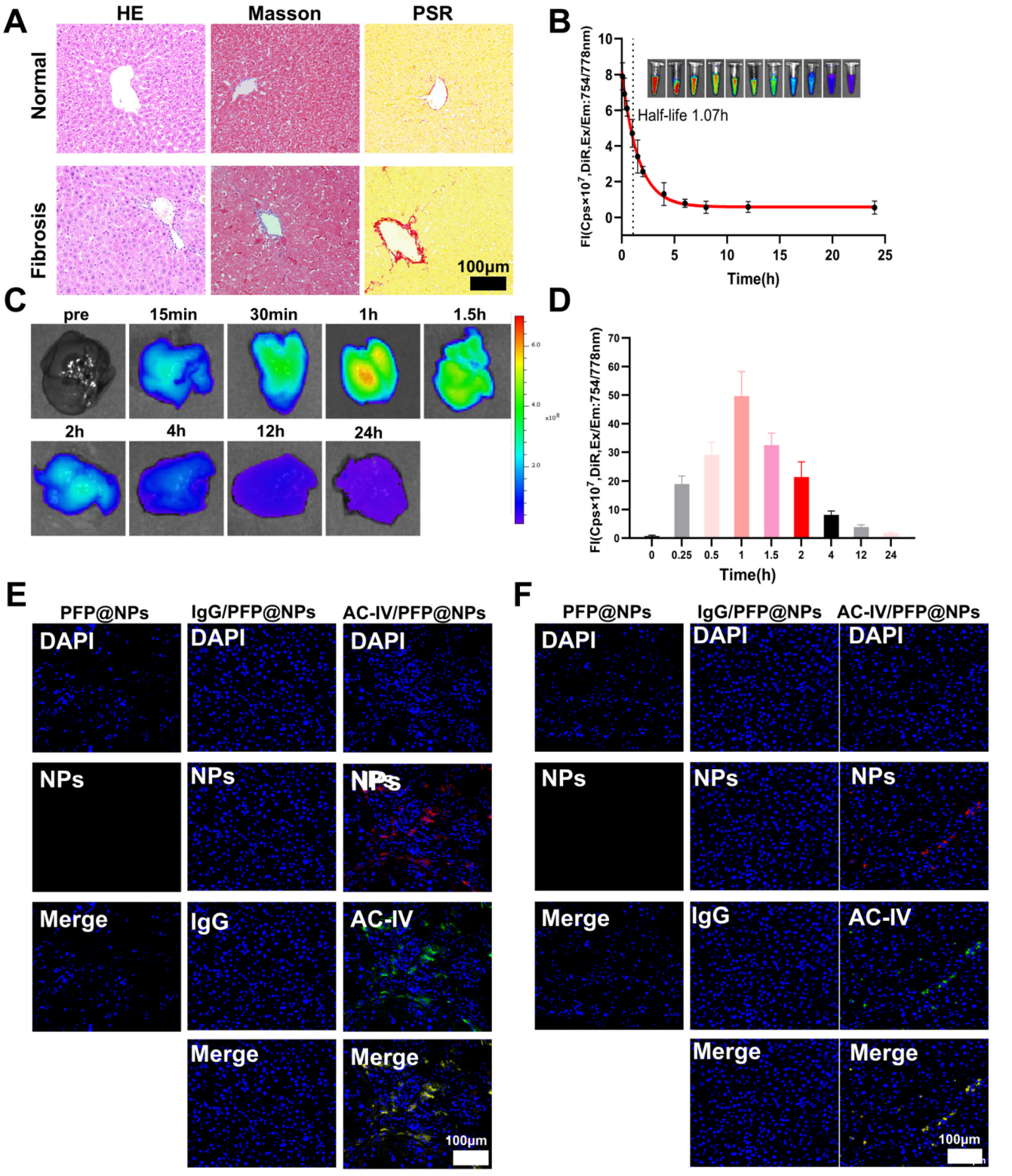

Fig. 4 *In vitro* and *in vivo* targeting of AC-IV-PFP@NPs in fibrotic liver tissue. (A) Histopathological analysis of normal and fibrotic liver tissues. (B) Pharmacokinetics of AC-IV-PFP@NPs labeled with DiR in the blood of healthy rats showing a gradual decrease in fluorescence intensity (n = 3). (C) Fluorescence images of fibrotic livers at different time points following the intravenous injection of DiR-labeled AC-IV-PFP@NPs. (D) Corresponding statistical analysis of the fluorescence intensity in the liver. (E) Confocal laser scanning microscopy images of cryosections from fibrotic liver tissue incubated with different nanoparticles. Nuclei were labeled with DAPI (blue), nanoparticles with DiI (red), and IgG and AC-IV with FITC (green). AC-IV-PFP@NPs showed positive staining, while IgG-PFP@NPs and PFP@NPs showed no signal (n = 6). Scale bar: 100 μm. (F) *In vivo* fluorescence imaging of frozen liver sections from rats injected intravenously with AC-IV-PFP@NPs or IgG-PFP@NPs (both labeled with DiI and FITC), or DiI-labeled PFP@NPs after 5 weeks of CCl_4 induction. Positive fluorescence was observed in the AC-IV-PFP@NP group only (n = 6). Scale bar: 100 μm.

sections. Fluorescence imaging revealed significantly reduced signals in the collagen-blocked group compared with the unblocked control (Fig. S4), confirming the specificity of AC-IV-mediated Col IV targeting.

Ultrasound molecular imaging of AC-IV-PFP@NPs

Ultrasound imaging parameters were optimized to maximize signal generation from AC-IV-PFP@NPs. *In vitro* gel phantom experiments demonstrated that LIFU irradiation at 3 W cm^{-2} for 3 min most effectively induced the liquid-to-gas phase transition of encapsulated perfluoropentane, producing abundant microbubbles that yielded peak B-mode and CEUS echo intensities (Fig. 5A, C and D). When these optimized parameters were applied *in vivo*, CEUS imaging of fibrotic rat livers revealed that echo intensity reached a maximum at 30 min after AC-IV-PFP@NP administration (16.67 ± 2.73; Fig. 5B and E; Table S1). This signal was significantly higher than that observed at other time points ($P < 0.001$) and significantly greater than that of non-targeted PFP@NPs. The temporal peak corresponded to the period of maximal nanoparticle accumulation within fibrotic regions, identifying the optimal imaging window and underscoring the role of active targeting in signal enhancement.

In vivo MFI varies with the progression of liver injury

Longitudinal CEUS monitoring of CCl_4-induced liver fibrosis demonstrated progressive changes in echo intensity, collagen deposition, and mean fluorescence intensity (MFI). Both CEUS

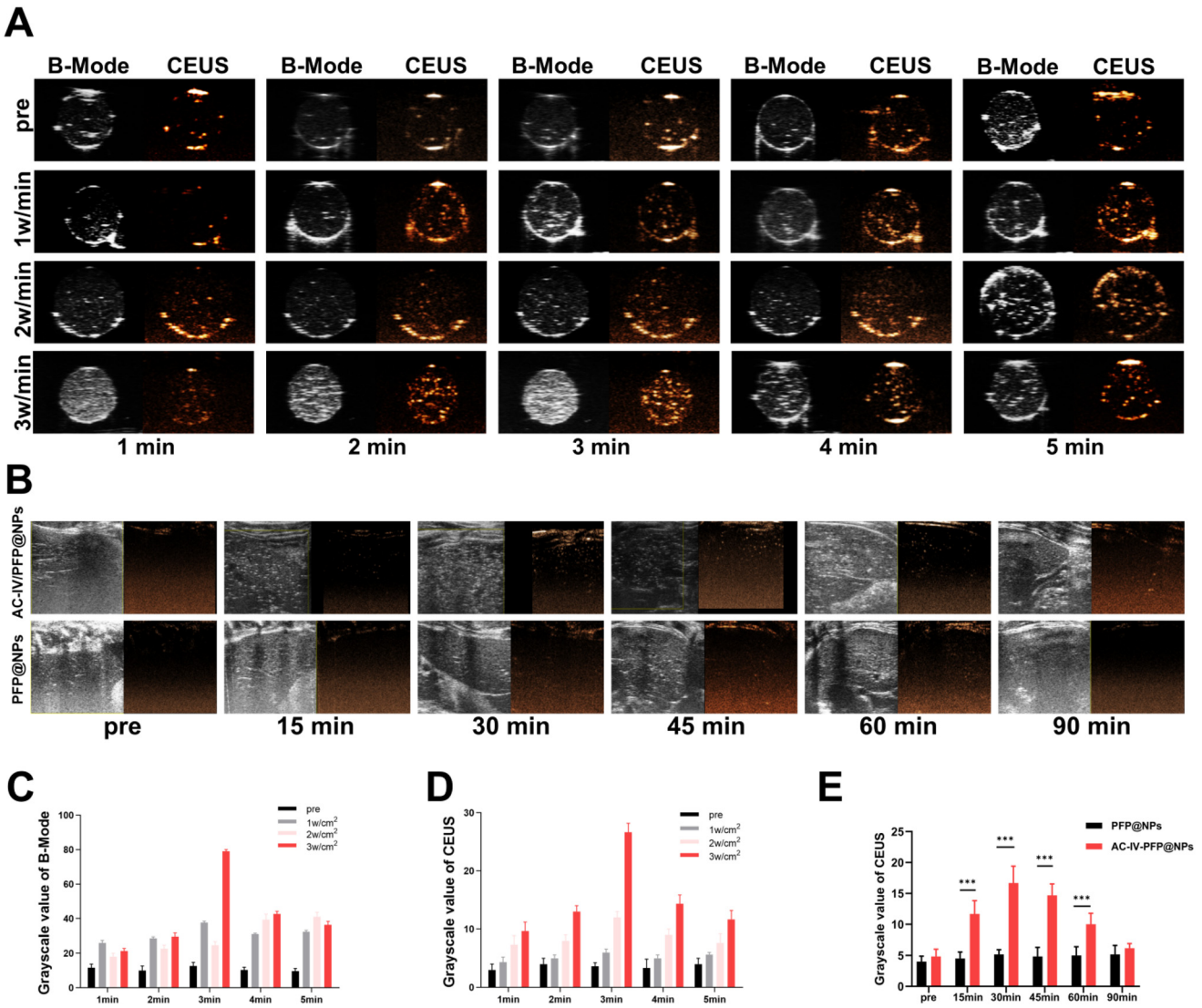

Fig. 5 *In vitro* and *in vivo* ultrasound imaging of AC-IV-PFP@NPs. (A) B-mode and contrast-enhanced ultrasound (CEUS) imaging of nanoparticles under different LIFU powers and exposure durations *in vitro*. (B) B-mode and CEUS imaging of rats with liver fibrosis following intravenous injection of AC-IV-PFP@NPs or PFP@NPs; signals were prominent at 30 min in the targeted (AC-IV-PFP@NPs) group. (C and D) Quantitative gray value analysis of the B-mode (C) and CEUS (D) imaging *in vitro*. (E) Time-course analysis of CEUS signal intensity *in vivo* (corresponding to panel E). *$P < 0.05$; **$P < 0.01$; and ***$P < 0.001$.

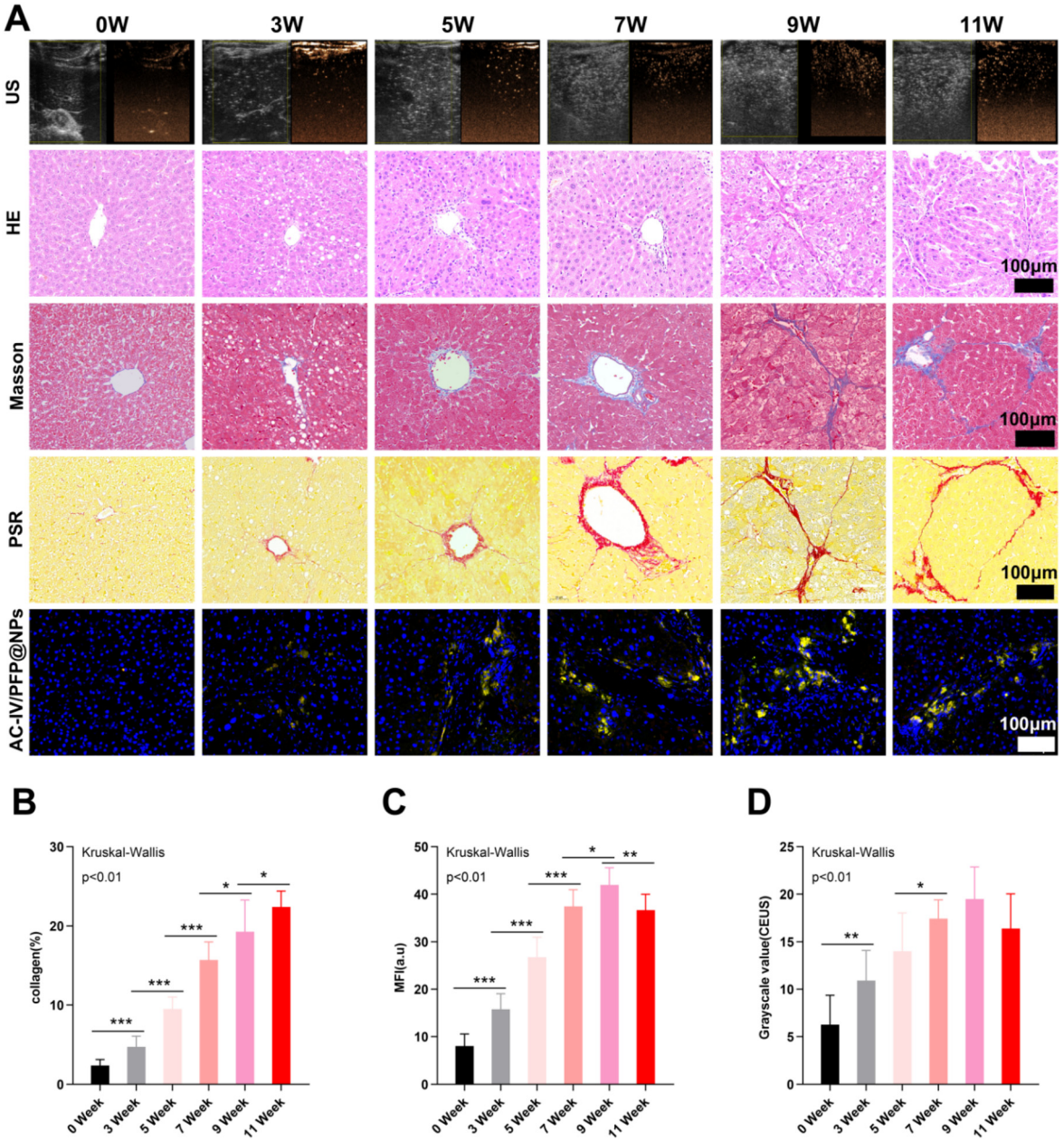

Fig. 6 Longitudinal evaluation of liver fibrosis progression using CEUS imaging. (A) CEUS imaging, histopathology, and mean fluorescence intensity (MFI) of liver tissues at 0, 3, 5, 7, 9, and 11 weeks following CCl_4 induction. Scale bar: 100 μm. (B–D) Semi-quantitative analysis of CEUS echogenicity intensity (B), collagen content (C), and MFI (D) in fibrotic *versus* control livers. *$P < 0.05$; **$P < 0.01$; and ***$P < 0.001$.

intensity and MFI increased in parallel with the duration of CCl_4 exposure, peaking at week 9 before declining at week 11, whereas collagen content exhibited a steady, linear increase (Fig. 6A–D; Table S2). The observed early increase in the CEUS signal and MFI corresponds to the phase of active type IV collagen deposition during fibrogenesis. However, the subsequent reduction at week 11 (Metavir stage S4, cirrhosis) likely reflects structural remodeling characterized by thick fibrous septa dominated by type I and III collagens, leading to a relative decline in type IV collagen abundance. These dense fibrillar networks limit nanoparticle penetration and mask type IV collagen epitopes, reducing AC-IV binding and microbubble formation, resulting in decreased CEUS signal intensity.[19] These findings indicate that while AC-IV-PFP@NPs enable sensitive detection of early and mid-stage fibrosis, their diagnostic performance may decrease in advanced disease due to structural barriers and altered collagen composition.

Accurate assessment of the progression of liver fibrosis

Stratification according to the METAVIR pathological staging system (S0–S4) further clarified the association between CEUS signal intensity and fibrosis severity. CEUS echo intensity dis-

played a significant stepwise increase from stage S0 (no fibrosis) through stage S3 (numerous septa without cirrhosis), followed by a decrease at stage S4 (cirrhosis) ($P < 0.05$; Fig. 7A–D and Table S3). Spearman correlation analysis revealed a strong positive correlation between CEUS intensity and fibrosis stage ($r = 0.725$, $P < 0.001$), while even higher correlations were

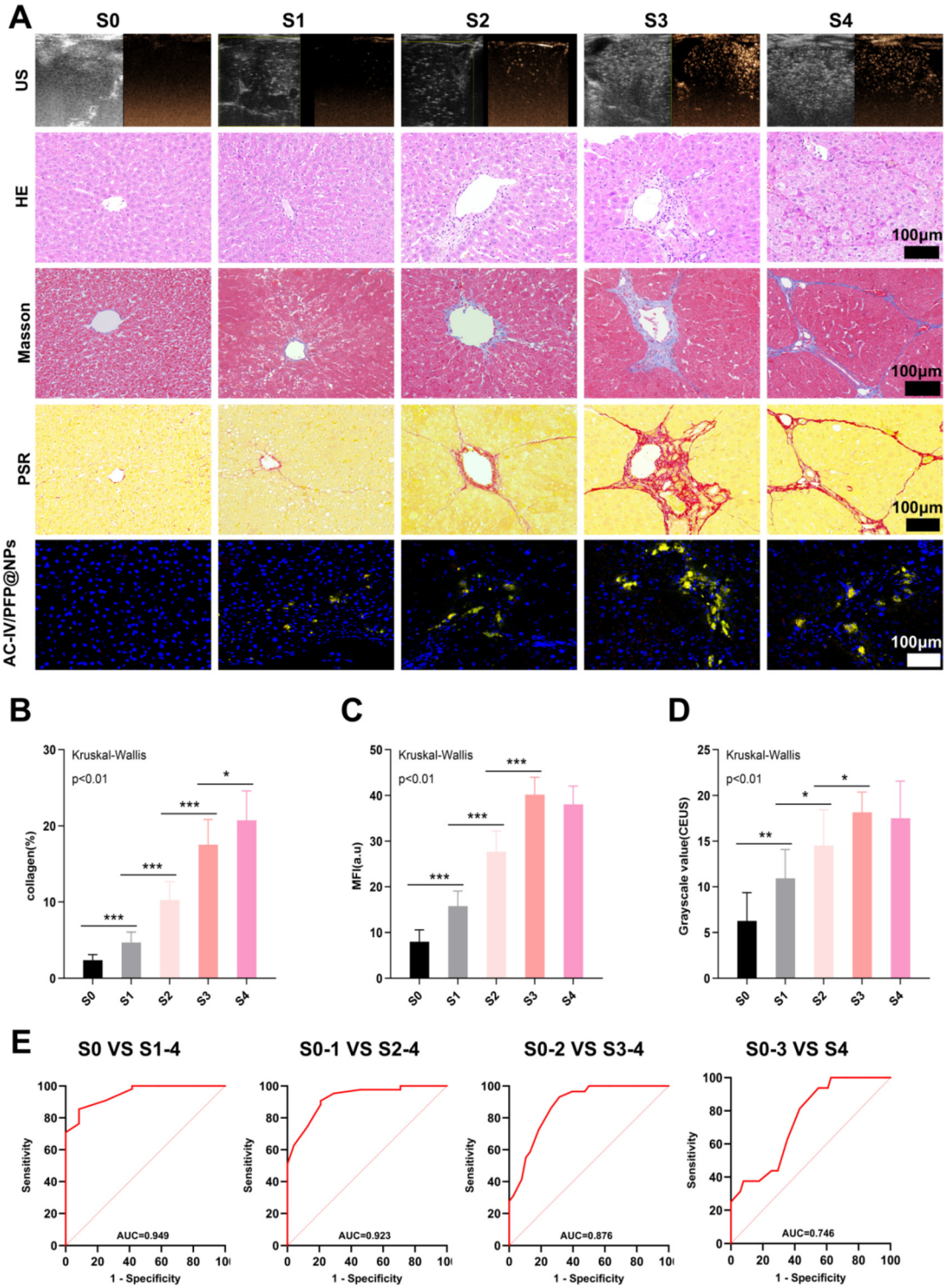

Fig. 7 CEUS-based staging of liver fibrosis. (A) CEUS imaging, histopathological evaluation, and MFI for fibrosis stages S0, S1, S2, S3, and S4. Scale bar: 100 μm. (B–D) Semi-quantitative comparisons of the collagen content (B), MFI (C), and CEUS echogenicity (D) across fibrosis stages. (E) ROC curve analysis demonstrating diagnostic performance of AC-IV-PFP@NP-based CEUS for staging liver fibrosis. AUC values for differentiating S0 *vs.* S1–S4, S0–S1 *vs.* S2–S4, S0–S2 *vs.* S3–S4, and S0–S3 *vs.* S4 were 0.949, 0.923, 0.876, and 0.746, respectively. *$P < 0.05$; **$P < 0.01$; and ***$P < 0.001$.

Table 1 Correlation analysis between CEUS echogenicity intensity, collagen content percentage, MFI, and liver fibrosis stages

Assessment parameters	*r*-Values	*P*-Values
CEUS grayscale values	0.725	0.000
Collagen (%)	0.94	0.000
MFI (a.u)	0.888	0.000

observed for collagen content percentage ($r = 0.940$, $P < 0.001$) and MFI ($r = 0.888$, $P < 0.001$) (Table 1). The strong correlation between MFI and histological staging highlights the specificity of AC-IV-PFP@NPs for type IV collagen. The moderate correlation for CEUS intensity may reflect limitations in ultrasound spatial resolution and signal attenuation effects in S4 cirrhosis.

The diagnostic performance of AC-IV-PFP@NP-based CEUS for fibrosis staging was assessed using the ROC curve analysis. The system demonstrated high diagnostic accuracy, particularly in early-stage detection. The differentiation between S0 and S1–S4 yielded an AUC of 0.949, with 85.5% sensitivity and 91.7% specificity at a cutoff of 9.5. Differentiation between S0–S1 and S2–S4 yielded an AUC of 0.923 (sensitivity: 90.7%, specificity: 79.2%, cutoff: 11.5) (Fig. 7E; Table 2). Classification between S0–S2 and S3–S4 remained robust (AUC: 0.876, cutoff: 13.5), whereas accuracy decreased for distinguishing S0–S3 from S4 (AUC: 0.746, cutoff: 12.5). These findings underscore the high sensitivity and specificity of AC-IV-PFP@NP-based UMI in detecting early fibrotic stages (S1–S2), characterized by elevated and accessible type IV collagen expression. The reduced diagnostic performance at stage S4 is consistent with the previously described attenuation in the CEUS signal, likely due to extensive deposition of type I and III collagen that physically limits nanoparticle penetration and obscures type IV collagen within the fibrotic septa. These observations suggest that multi-targeted strategies may be required to accurately assess advanced-stage fibrosis.

Discussion

In this study, liquid–gas phase-change nanoparticles (AC-IV-PFP@NPs) were prepared by conjugating AC-IV antibodies to the nanoparticle surface and encapsulating PFP, enabling active targeting of type IV collagen in liver tissue and facilitating UMI of liver fibrosis. The results demonstrated that AC-IV-PFP@NPs selectively accumulated in fibrotic regions of the liver in rats, with their distribution positively correlated with fibrosis severity (Pearson $r = 0.888$). The CEUS echo intensity values also showed a positive correlation with fibrosis stage (Pearson $r = 0.725$). The diagnostic performance of AC-IV-PFP@NPs for early liver fibrosis was high, with AUCs of 0.949 and 0.923 for differentiating S0 *vs.* S1–S4 and S0–S1 *vs.* S2–S4, respectively. Both CEUS echo intensity and MFI declined slightly in advanced fibrosis (S4), and the diagnostic performance for S0–S3 *vs.* S4 (AUC = 0.746) was significantly lower than that for earlier stages. This decline may be attributed to several factors. First, repeated hepatocellular injury, abnormal fibrotic proliferation, and capillarization of hepatic sinusoids during fibrosis progression reduce the number and diameter of fenestrae in liver sinusoidal endothelial cells (LSECs), inhibiting nanoparticle penetration into the fibrotic parenchyma.[25,26] Second, although type IV collagen increases significantly in early fibrosis, its relative abundance reduces in later stages due to the excessive accumulation of interstitial collagens, such as type I and type III collagen.[21] These findings suggest that AC-IV-PFP@NPs are more suitable for imaging and staging early liver fibrosis. For advanced fibrosis, a multi-target approach incorporating probes directed at type I collagen or fibrosis-related cytokines may improve diagnostic accuracy.

A key advantage of AC-IV-PFP@NPs lies in their ability to specifically bind to type IV collagen in fibrotic liver tissue. In a normal liver, type IV collagen is sparsely distributed.[27] However, as fibrosis progresses, the space of Disse transforms into a basement membrane-like structure, and type IV collagen content increases significantly. Previous studies have shown that type IV collagen is significantly upregulated during the initial phases of liver fibrosis and appears earlier than type I and III collagen.[14–16,28] These characteristics underscore the utility of type IV collagen as a promising biomarker for early-stage liver fibrosis.

Currently, most probes used for the diagnosis of liver fibrosis target molecular markers associated with fibrogenesis, such as fibroblast activation protein (FAP),[29] collagen I,[30–32] and integrin αvβ3.[33,34] For example, Song *et al.*[29] reported a FAP-targeted probe with AUC values of 0.859 and 0.845 for distinguishing fibrosis stages $S \leq 1$ *vs.* $S \geq 2$ and $S \leq 2$ *vs.* $S \geq 3$, respectively (METAVIR system). In this study, liver CEUS echo intensity values demonstrated better diagnostic efficacy for fibrosis staging (S0–S1 *vs.* S2–S4 and S0–S2 *vs.* S3–S4), with AUC values of 0.923 and 0.876, respectively. Balachandran *et al.*[31] developed heterogeneous iron oxide/dysprosium oxide nanoparticles (IO-DyO NPs) targeting collagen I, achieving an AUC of 0.92 for differentiating early (Ishak stages 1–2) from intermediate fibrosis (stages 3–4), with diagnostic accuracy comparable to that of this study. However, this study provides more refined stratification by assessing four discrete staging thresholds (Table 2). While several studies have confirmed the utility of collagen I-targeted probes in animal models of liver fibrosis,[30–32] the advantage of collagen I as a marker is limited in early-stage fibrosis compared to type IV collagen. Zhang *et al.* developed collagen I-targeting iron oxide nanoparticles (SNIO–CBP) for rapid, low-dose imaging; however, their ability

Table 2 Diagnostic efficacy of CEUS echogenicity intensity for liver fibrosis staging

Liver fibrosis stages	AUC	Cutoff values	Sensitivity (%)	Specificity (%)
S0 *vs.* S1–S4	0.949	9.5	85.5	91.7
S0–S1 *vs.* S2–S4	0.923	11.5	90.7	79.2
S0–S2 *vs.* S3–S4	0.876	13.5	93.1	68.4
S0–S3 *vs.* S4	0.746	12.5	93.8	45.1

to detect early-stage liver fibrosis remains limited.[35] Other studies have investigated alternative molecular targets such as CD44 and integrin αvβ3.[33,34,36] Hu *et al.* designed iron oxide nanoparticles functionalized with cRGD peptides to specifically bind to integrin αvβ3 on HSCs, enabling the precise staging of liver fibrosis.[34] Similarly, Wu *et al.* synthesized $NaGdF_4$@PEG@HA nanoprobes that target HSCs through CD44 binding, achieving noninvasive and accurate fibrosis diagnosis.[37] Despite these advances, the broad expression of these biomarkers limits their specificity.

Integrin αvβ3 is also expressed in vascular endothelial cells and inflammatory cells, including monocytes and macrophages.[38] CD44 is overexpressed on multiple tumor cell types and is also found in other organs such as the liver, kidneys, and spleen.[36,39] These findings suggest that type IV collagen provides higher target specificity for liver fibrosis diagnosis. Furthermore, type IV collagen is a key basement membrane component present in fibrotic lesions. Its expression reflects ECM deposition during fibrosis and shows higher diagnostic specificity and sensitivity in early-stage liver fibrosis.[40]

Other advantages of AC-IV-PFP@NPs include their robust UMI performance. Upon LIFU activation, the encapsulated PFP undergoes phase transition, producing microbubbles and significantly increasing CEUS signal intensity. This allows quantifiable, real-time detection of early fibrotic changes. AC-IV-PFP@NPs showed excellent performance in diagnosing early-stage fibrosis (S0–S2), a phase where conventional imaging often lacks sensitivity. For comparison, Cao *et al.*[41] reported AUC values of 0.851 and 0.830 for liver stiffness measurements (LSM) in identifying fibrosis stages $F \geq 1$ and $F \geq 2$, respectively. Miao *et al.*[42] investigated UMI and two-dimensional shear wave elastography (2D SWE) in 120 rats with different fibrosis degrees. UMI targeting CD34 was more accurate than 2D SWE in diagnosing early fibrosis (AUC: 0.97 *vs.* 0.82). Song *et al.*[29] also applied positron emission tomography (PET) imaging using an FAP-targeted tracer for fibrosis staging in rats. However, PET cannot resolve anatomical structures and relies on radiotracers, limiting its clinical application.[43] Magnetic resonance molecular imaging with targeted probes has been explored as a non-invasive approach. Although MRI offers high resolution and soft tissue contrast, it is more effective for moderate to advanced stages and lacks sensitivity in early fibrosis detection. To further improve diagnostic resolution, gadolinium-based dynamic contrast-enhanced MRI (DCE-MRI) is often used; however, it is contraindicated in patients with renal failure.[7] Ultrasound imaging presents several advantages, including cost-effectiveness, real-time capability, dynamic observation, and suitability for bedside application.[44] Therefore, this study established a UMI approach using type IV collagen-targeted nanoprobes (AC-IV-PFP@NPs) as tracers for liver fibrosis staging, which has demonstrated excellent diagnostic accuracy for early-stage fibrosis, addressing an important gap in current diagnostic tools.

Beyond imaging-based diagnostics, the evaluation of liver fibrosis also includes serum biomarkers and elastography techniques, each with distinct advantages and limitations. Serum biomarkers, such as FIB-4 and aspartate aminotransferase-to-platelet ratio index (APRI), offer a simple and low-cost means of assessment but lack spatial resolution and are influenced by inflammatory conditions.[45] Elastography modalities, including FibroScan and shear-wave imaging, provide quantitative measurements of tissue stiffness and perform well in advanced fibrosis; however, their sensitivity and specificity in early-stage disease are limited, and they cannot effectively differentiate between inflammation and fibrotic remodeling.[46,47] In contrast, the Col IV-targeted phase-change nanoparticles (AC-IV-PFP@NPs) developed in this study enable molecular-level detection of extracellular matrix remodeling, allowing for early and spatially resolved visualization of fibrotic changes through standard ultrasound systems. This molecular specificity provides a significant advantage in identifying reversible stages of fibrosis (S1 and S2).

Although this study presents several important findings, certain limitations require attention. First, the sample size across different stages of liver fibrosis was relatively limited, requiring larger cohorts to improve statistical power and diagnostic reliability. Second, in clinical settings, liver fibrosis arises from various etiologies, including viral infections (*e.g.*, HBV, HCV), alcohol consumption, drug toxicity, and environmental toxins,[2,48] which share a common pathogenic basis involving hepatocellular degeneration and necrosis, which in turn lead to fibrogenesis. Although the CCl_4-induced model used in this study aligns with the basic pathogenic mechanisms, it does not fully recapitulate the complexity of clinical fibrosis.[21] Third, while the nanoparticles effectively targeted type IV collagen, the effects of other pathological microenvironmental components, including inflammatory cytokines and immune cell infiltration, remain to be elucidated.[49] Furthermore, although the observed reduction in Col IV signal aligns with published evidence on extracellular matrix remodeling,[21,50–52] direct experimental confirmation of the proposed shielding mechanism is still required. Future studies should employ multiplex immunohistochemistry or advanced imaging methods to visualize and quantify the spatial colocalization of collagens I, III, and IV, confirming their interactive contributions during fibrosis progression. While the AC-IV-PFP@NPs developed in this study exhibited strong targeting and diagnostic capabilities, several challenges remain for clinical translation. Process optimization for large-scale production, along with standardized manufacturing under Good Manufacturing Practice (GMP) conditions, will be critical for clinical feasibility. Thus, future research should include expanded sample sizes, develop liver fibrosis models that more closely reflect clinical etiologies, investigate the interaction between nanoparticles and the fibrotic microenvironment in more depth, and focus on conducting comprehensive preclinical safety and efficacy evaluations in large animal models. Moreover, multi-targeted nanoparticles should be designed to complement type IV collagen-based detection, improving diagnostic coverage across the full fibrosis spectrum, from early to advanced stages. The AC-IV-PFP@NP platform holds promise for integration into a theranostic system. By incorporating anti-fibrotic agents, this nanoplatform could enable simul-

taneous precision diagnosis and treatment, improving its translational and clinical value.

Conclusion

This study demonstrates that type IV collagen-targeted phase-change nanoparticles represent an effective and highly specific platform for ultrasound molecular imaging-based staging of liver fibrosis, with particular sensitivity in early-stage detection. The diagnostic performance over conventional methods, such as FibroScan and serological assays, is attributed to active molecular targeting of a pathologically upregulated ECM component in early fibrogenesis. Although MRI-based molecular imaging offers better spatial resolution, ultrasound imaging provides key advantages in terms of real-time monitoring, cost-effectiveness, and the absence of ionizing radiation. The reduction in imaging signal observed in advanced fibrosis (S4) likely reflects ECM remodeling, including the predominance of type I/III collagen and architectural barriers to nanoparticle access. To overcome this, future studies should explore multi-targeted nanoparticle platforms or optimize nanoparticle penetration in dense fibrotic tissue. Translation to large-animal models and clinical studies is essential for validating this platform's utility in non-invasive liver fibrosis assessment and therapeutic monitoring.

Author contributions

Y. Long and S. Zhong: conception, design, data analysis, and writing; F. Li, W. Zhang, and Y. Hu: methodology, validation, and investigation; M. Dai and M. Zheng: project administration and validation; L. Cheng and H. Ran: supervision, funding acquisition, and writing – review & editing.

Conflicts of interest

There are no conflicts to declare.

Ethics approval statement

All animal experiments were in accordance with the Guide for Care and Use of Laboratory Animals and approved by the Animal Ethics Committee of Chongqing Medical University (acceptance number: IACUC-CQMU-2024-01037).

Data availability

All the data related to the study are available at: https://doi.org/10.5281/zenodo.16745955.

Supplementary information (SI) is available. See DOI: https://doi.org/10.1039/d5bm01181g.

Acknowledgements

This work was financially supported by the Chongqing Natural Science Foundation of China (CSTB2022NSCQ-MSX1580) and the Program of Chongqing Health Commission and Chongqing Science and Technology Bureau Joint Medical Research Project (2023MSXM061).

References

1 P. Horn and F. Tacke, *Cell Metab.*, 2024, **36**, 1439–1455.
2 J. Rao, H. Wang, M. Ni, Z. Wang, Z. Wang, S. Wei, M. Liu, P. Wang, J. Qiu, L. Zhang, C. Wu, H. Shen, X. Wang, F. Cheng and L. Lu, *Gut*, 2022, **71**, 2539–2550.
3 F. He, W. N. Li, X. X. Li, K. Y. Yue, J. L. Duan, B. Ruan, J. J. Liu, P. Song, Z. S. Yue, K. S. Tao and L. Wang, *Theranostics*, 2022, **12**, 1816–1828.
4 G. Xie, X. Wang, R. Wei, J. Wang, A. Zhao, T. Chen, Y. Wang, H. Zhang, Z. Xiao, X. Liu, Y. Deng, L. Wong, C. Rajani, S. Kwee, H. Bian, X. Gao, P. Liu and W. Jia, *BMC Med.*, 2020, **18**, 144.
5 N. Kawamura, K. Imajo, K. J. Kalutkiewicz, K. Nagai, M. Iwaki, T. Kobayashi, A. Nogami, Y. Honda, T. Kessoku, Y. Ogawa, T. Higurashi, K. Hosono, H. Takahashi, M. Yoneda, S. Saito, S. Aishima, H. Toyoda, H. Hayashi, Y. Sumida, R. L. Ehman and A. Nakajima, *Hepatology*, 2022, **76**, 186–195.
6 L. A. Adams, M. Thiele and E. A. Tsochatzis, *Hepatology*, 2025, DOI: 10.1097/HEP.0000000000001400.
7 S. Chen, D. Zhuang, Q. Jia, B. Guo and G. Hu, *Biomater. Res.*, 2024, **28**, 0042.
8 S. M. van de Looij, E. R. Hebels, M. Viola, M. Hembury, S. Oliveira and T. Vermonden, *Bioconjugate Chem.*, 2022, **33**, 4–23.
9 M. A. Heneghan, E. Shumbayawonda, A. Dennis, R. Z. Ahmed, M. N. Rahim, M. Ney, L. Smith, M. Kelly, R. Banerjee and E. L. Culver, *eClinicalMedicine*, 2022, **46**, 101325.
10 A. J. Sanyal, L. Castera and V. W.-S. Wong, *Clin. Gastroenterol. Hepatol.*, 2023, **21**, 2026–2039.
11 R. Guo, X. Jia, Z. Ding, G. Wang, M. Jiang, B. Li, S. Chen, B. Xia, Q. Zhang, J. Liu, R. Zheng, Z. Gao and X. Xie, *Theranostics*, 2022, **12**, 5220–5236.
12 S. Chen, D. Zhuang, Q. Jia, B. Guo and G. Hu, *Biomater. Res.*, 2024, **28**, 0042.
13 Q. Yang, J. Peng, C. Chen, Y. Xiao, L. Tan, X. Xie, X. Xu and Z. Qian, *J. Biomed. Nanotechnol.*, 2018, **14**, 1208–1224.
14 L. Nian, W. Li, C. Zhang, L. Li, G. Zhang and J. Xiao, *ACS Sens.*, 2024, **9**, 3272–3281.
15 W. D. Du, Y. E. Zhang, W. R. Zhai and X. M. Zhou, *World J. Gastroenterol.*, 1999, **5**, 397–403.
16 I. Lønsmann, J. I. Grove, A. Haider, P. Kaye, M. A. Karsdal, D. J. Leeming and G. P. Aithal, *Biology*, 2023, **12**, 1087.
17 Q. Wang, T. Lu, P. Song, Y. Dong, C. Dai, W. Zhang, X. Jia, Z. Guo, M. Zhao, J. Zhang, P. Wang, J. Wang and Q. Guo, *Phytomedicine*, 2024, **133**, 155878.

18 T. K. Kim, S. Y. Noh, S. R. Wilson, Y. Kono, F. Piscaglia, H.-J. Jang, A. Lyshchik, C. F. Dietrich, J. K. Willmann, A. Vezeridis and C. B. Sirlin, *Clin. Mol. Hepatol.*, 2017, **23**, 280–289.
19 T. Eom, J. H. Park, J. Y. Pyun, M. Park, J. Lee, E. Park, W. Choi, S. Han, S. Lee, B. C. Lee and D. Yoo, *ACS Appl. Mater. Interfaces*, 2025, **17**, 37562–37576.
20 F. Li, L. Chen, S. Zhong, J. Chen, Y. Cao, H. Yu, H. Ran, Y. Yin, C. Reutelingsperger, S. Shu and Z. Ling, *ACS Nano*, 2024, **18**, 4886–4902.
21 M. A. Karsdal, S. H. Nielsen, D. J. Leeming, L. L. Langholm, M. J. Nielsen, T. Manon-Jensen, A. Siebuhr, N. S. Gudmann, S. Rønnow, J. M. Sand, S. J. Daniels, J. H. Mortensen and D. Schuppan, *Adv. Drug Delivery Rev.*, 2017, **121**, 43–56.
22 N. K. Lee, C. J. Wang, J. Lim, W. Park, H. K. Kwon, S. N. Kim, T. H. Kim and C. G. Park, *Nano Convergence*, 2021, **8**, 24.
23 S. Xu, Y. Chen, J. Miao, Y. Li, J. Liu, J. Zhang, J. Liang, S. Chen and S. Hou, *Phytomedicine*, 2024, **128**, 155465.
24 S. Mahalunkar, A. S. Yadav, M. Gorain, V. Pawar, R. Braathen, S. Weiss, B. Bogen, S. W. Gosavi and G. C. Kundu, *Int. J. Nanomed.*, 2019, **14**, 8285–8302.
25 L. F. Zhang, X. H. Wang, C. L. Zhang, J. Lee, B. W. Duan, L. Xing, L. Li, Y. K. Oh and H. L. Jiang, *ACS Nano*, 2022, **16**, 14029–14042.
26 T. Li, W. Fu, X. Li, Y. Huo, H. Ji, T. Liang and R. Zhang, *ACS Appl. Mater. Interfaces*, 2025, **17**, 386–397.
27 H. Nyström, *Semin. Cancer Biol.*, 2021, **71**, 134–142.
28 A. Niu and T. Qi, *Ann. Transl. Med.*, 2022, **10**, 1310.
29 Y. Song, C. Qin, Y. Chen, W. Ruan, Y. Gai, W. Song, Y. Gao, W. Hu, P. Qiao, X. Song, X. Lv, D. Zheng, H. Chu, D. Jiang, L. Yang and X. Lan, *Eur. J. Nucl. Med. Mol. Imaging*, 2024, **51**, 3572–3584.
30 M. Salarian, R. C. Turaga, S. Xue, M. Nezafati, K. Hekmatyar, J. Qiao, Y. Zhang, S. Tan, O. Y. Ibhagui, Y. Hai, J. Li, R. Mukkavilli, M. Sharma, P. Mittal, X. Min, S. Keilholz, L. Yu, G. Qin, A. B. Farris, Z.-R. Liu and J. J. Yang, *Nat. Commun.*, 2019, **10**, 4777.
31 Y. L. Balachandran, W. Wang, H. Yang, H. Tong, L. Wang, F. Liu, H. Chen, K. Zhong, Y. Liu and X. Jiang, *ACS Nano*, 2022, **16**, 5647–5659.
32 J. Zhang, Y. Ning, H. Zhu, N. J. Rotile, H. Wei, H. Diyabalanage, E. C. Hansen, I. Y. Zhou, S. C. Barrett, M. Sojoodi, K. K. Tanabe, V. Humblet, A. Jasanoff, P. Caravan and M. G. Bawendi, *Proc. Natl. Acad. Sci. U. S. A.*, 2023, **120**, e2220036120.
33 J. Cui, G. Wang, L. X. Yip, M. Dong, M. Mu, L. Tian, Y. Gao, Q. Fan, Q. Zhu, X. Zhao, X. Xu, D. T. Leong and X. Sun, *Adv. Funct. Mater.*, 2024, **34**, DOI: 10.1002/adfm.202410748.
34 Q. Hu, Y. Su, S. Ma, P. Wei, C. He, D. Yang, Y. Qian, Y. Shen, X. Zhou, Z. Zhou and H. Hu, *ACS Appl. Mater. Interfaces*, 2024, **16**, 2012–2026.
35 J. Zhang, Y. Ning, H. Zhu, N. J. Rotile, H. Wei, H. Diyabalanage, E. C. Hansen, I. Y. Zhou, S. C. Barrett, M. Sojoodi, K. K. Tanabe, V. Humblet, A. Jasanoff, P. Caravan and M. G. Bawendi, *Proc. Natl. Acad. Sci. U. S. A.*, 2023, **120**, e2220036120.
36 J. Shinn, S. Park, S. Lee, N. Park, S. Kim, S. Hwang, J. J. Moon, Y. Kwon and Y. Lee, *ACS Nano*, 2024, **18**, 4704–4716.
37 S. Wu, T. Xu, J. Gao, Q. Zhang, Y. Huang, Z. Liu, X. Hao, Z. Yao, X. Hao, P. Y. Wu, Y. Wu, B. Yin and Z. Tang, *Eur. J. Nucl. Med. Mol. Imaging*, 2024, **52**, 48–61.
38 L. Pan, P. Bai, X. Weng, J. Liu, Y. Chen, S. Chen, X. Ma, K. Hu, A. Sun and J. Ge, *Circulation*, 2022, **145**, 659–674.
39 J. Ge, M. Zuo, Q. Wang and Z. Li, *J. Nanobiotechnol.*, 2023, **21**, 48.
40 C. Gan, U. Yaqoob, J. Lu, M. Xie, A. Anwar, N. Jalan-Sakrikar, S. Jerez, T. S. Sehrawat, A. Navarro-Corcuera, E. Kostallari, N. W. Habash, S. Cao and V. H. Shah, *JCI Insight*, 2024, **9**, e174775.
41 Y. T. Cao, L. L. Xiang, F. Qi, Y. J. Zhang, Y. Chen and X. Q. Zhou, *eClinicalMedicine*, 2022, **51**, 101547.
42 X. Miao, T. Sha, W. Zhang, H. Zhou, C. Qiu, H. Deng, Y. You, J. Ren, X. Zhang, R. Zheng and T. Yin, *Radiology*, 2022, **304**, 473–482.
43 L. Zhao, F. Kang, Y. Pang, J. Fang, L. Sun, H. Wu, X. Lan, J. Wang and H. Chen, *J. Nucl. Med.*, 2024, **65**, 4S–11S.
44 M. A. Gómez-Bermejo, D. Y. Huang, M. Bertolotto and P. S. Sidhu, *Insights Imaging*, 2023, **14**, 158.
45 Y. Vali, J. Lee, J. Boursier, S. Petta, K. Wonders, D. Tiniakos, P. Bedossa, A. Geier, S. Francque, M. Allison, G. Papatheodoridis, H. Cortez-Pinto, R. Pais, J. F. Dufour, D. J. Leeming, S. A. Harrison, Y. Chen, J. F. Cobbold, M. Pavlides, A. G. Holleboom, H. Yki-Jarvinen, J. Crespo, M. Karsdal, R. Ostroff, M. H. Zafarmand, R. Torstenson, K. Duffin, C. Yunis, C. Brass, M. Ekstedt, G. P. Aithal, J. M. Schattenberg, E. Bugianesi, M. Romero-Gomez, V. Ratziu, Q. M. Anstee and P. M. Bossuyt, *Lancet Gastroenterol. Hepatol.*, 2023, **8**, 714–725.
46 W. Huang, Y. Peng and L. Kang, *VIEW*, 2024, **5**, 20240010.
47 Y. Wang, X. Yang and S. Wang, *Arch. Med. Sci.*, 2024, **20**, 1784–1792.
48 M. Parola and M. Pinzani, *Mol. Aspects Med.*, 2024, **95**, 101231.
49 B. Chakraborty, R. Pal, M. Ali, L. M. Singh, D. Shahidur Rahman, S. Kumar Ghosh and M. Sengupta, *Cell. Mol. Immunol.*, 2016, **13**, 191–205.
50 K. Böttcher and M. Pinzani, *Adv. Drug Delivery Rev.*, 2017, **121**, 3–8.
51 A. Khurana, N. Sayed, P. Allawadhi and R. Weiskirchen, *Ann. Transl. Med.*, 2021, **9**, 728.
52 A. Brougham-Cook, I. Jain, D. A. Kukla, F. Masood, H. Kimmel, H. Ryoo, S. R. Khetani and G. H. Underhill, *Acta Biomater.*, 2022, **138**, 240–253.